PHOTONICS Research

Plasmonic vortex beam emitter

Zi-Wen Zhang,[1,2] Yu-Lu Lei,[1,2] Juan-Feng Zhu,[3] and Chao-Hai Du[1,2,*]

[1]Center for Carbon-based Electronics, School of Electronics, Peking University, Beijing 100871, China
[2]State Key Laboratory of Advanced Optical Communication Systems and Networks, School of Electronics, Peking University, Beijing 100871, China
[3]Science, Mathematics, and Technology (SMT), Singapore University of Technology and Design, Singapore 487372, Singapore
*Corresponding author: duchaohai@pku.edu.cn

Received 7 June 2023; revised 2 August 2023; accepted 3 August 2023; posted 3 August 2023 (Doc. ID 497533); published 27 September 2023

Terahertz vortices prompt numerous advanced applications spanning classical and quantum communications, sensing, and chirality-based detection, owing to the inherent physical properties of terahertz waves and orbital angular momentum (OAM). Nonetheless, existing methodologies for generating terahertz vortices face challenges such as unalterable topological charges and intricate feed networks. To address these limitations, we propose a novel approach to generate multi-mode and tunable vortex beams based on chiral plasmons. Through eigenmode analysis, the uniform helical gratings are demonstrated to support chiral plasmons carrying OAM. By leveraging their vortex characteristics and introducing modulation into the periodic system, these chiral plasmons are alternatively diffracted into high-purity vortex radiations according to the Bragg law. To validate the theory, the vortex beam emitter is fabricated and measured in the microwave regime based on the modulated scheme. Experimental results confirm the emission of vortex beams with desirable phase distributions and radiation patterns. Our findings highlight the potential of chiral plasmons as seeds for tunable and compact vortex radiation, offering promising applications in tunable vortex sources.

https://doi.org/10.1364/PRJ.497533

1. INTRODUCTION

The angular momentum of photons encompasses both spin and orbital components, which are related to the polarization and wavefront distributions of electromagnetic waves. In contrast to the limited states of spin angular momentum, such as right and left rotations, orbital angular momentum (OAM) exhibits an infinite range of states, spanning from negative infinity to positive values, as demonstrated in seminal work by Allen *et al.* [1]. Exploiting the advantages of OAM, such as topological protection and mode orthogonality within different quantum states [2,3], optical vortex photons have found numerous applications in optical tweezers [4], communications [5], quantum entanglement [6], and nonlinear optics [7]. Extending optical vortices into the terahertz (THz) band, leveraging the broadband and unique properties of THz waves, further promotes the development of THz communications [8] and chiral spectroscopy [9]. As a result, significant efforts have been dedicated by the community toward generating high-performance THz vortex beams. However, achieving tunable vortex beams over a broad range remains an urgent need for advanced multi-mode and high-purity applications. The spiral phase plate is first proposed to apply helical phase constraint for the incident Gaussian beam, where the topological charge (TC) is structurally limited to certain values without tunability in OAM and operation band [10]. Inspired by holographic optical photonics, a computer-assisted THz hologram has been fabricated to spatially govern the in-plane phased distributions of the incident beam, whereas their tunability is still limited [11]. Through the advancement and miniaturization of metamaterials, the V-shaped slits have been tailored to function as vortex plates, precisely designed to operate at frequencies that align with the structural resonant frequencies [12]. Based on the comparable mechanism, emission of nondiffractive Bessel vortex beams at 2.13 THz has been achieved through the implementation of Fresnel spiral plates, which have been experimentally demonstrated using the Novosibirsk free-electron lasers [13,14]. Furthermore, the conversion of radially polarized beams into high-power and broadband vortex beams has been realized through the use of achromatic elements across the frequency range of 0.75 to 2 THz [15]. To summarize, these methodologies have been meticulously crafted to manifest THz vortices with a precise TC at either a singular frequency or within narrow bandwidths. However, the constrained tunability of the TC and the narrow operating bands pose limitations on their potential for advanced multi-mode applications. To surmount these obstacles, the utilization of chiral plasmonics carrying OAMs holds immense promise, offering a potential solution for achieving a tunable TC separately in multiple narrow bands.

Spoof surface plasmons (SSPs) are artificial counterparts of optical surface plasmons that operate across the microwave to infrared bands by leveraging structural periodic systems [16].

Remarkably, these plasmons eliminate the requirement for metals with negative permittivity, presenting a novel avenue for replicating the behavior of natural plasmons [17]. Due to their dispersion relations exhibiting large longitudinal wave vectors, these mimicking modes exhibit near-field local effects and transverse surface-field enhancement. Consequently, they enable compact and intense applications in the THz bands, including integrated plasmonic sensors and waveguides [18–20], subwavelength focusing [21], and far-field optical hyperlens [22]. Advancements in material topology and functional requirements have led to the evolutionary development of distinctive plasmonic modes characterized by their structural and functional properties [23]. Examples include planar SSPs [24], conformal SSPs [24], and localized SSPs [24]. Among this diverse range of SSPs, chiral ones offer inherent versatility for achieving tunable vortex radiation, as they naturally carry OAMs associated with different mode orders [25]. In efforts to generate vortex beams, a compound scheme has been devised where supplemental diffraction structures are placed around the helical grating, resulting in the emission of multi-mode vortex radiation [26]. However, this approach necessitates an additional concentric diffractive structure, which poses challenges to practical robustness. Consequently, the exploration of a scheme for diffracting localized chiral plasmons into vortex beams remains an active area of research. Promisingly, the implementation of periodic modulations holds potential in overcoming this hurdle [27–29]. While vortex free-electron radiation based on chiral plasmons can generate tunable vortex beams, the constraints associated with generating symmetry-customized electron beams pose challenges in the design of electron optical systems and dynamic vacuum systems [29]. As a result, it remains a considerable distance away from practical applications and development into a high-performance vortex beam generator. Therefore, the exploration of engineering-feasible and implementable generators that enable the creation of multi-mode and tunable vortex beams remains an ongoing pursuit. Such research would undoubtedly make a substantial and valuable contribution to THz spectroscopy and communication.

Here, a novel approach is presented for the design of a compact and tunable vortex beam emitter that leverages chiral plasmons with separate OAMs. Through eigenmode analysis, the presence of distinct TCs carried by the photons is revealed by the spiral wavefronts observed in the spatial phase distributions in real space. To achieve the desired properties, double-period depth modulation is incorporated into the proposed helical periodic systems, enabling a gentle phase-matching condition between the chiral plasmons and free space, as dictated by the fundamental principle of the Bragg law. Consequently, vortex beams with desired TCs are alternatively generated as the frequency increases. Furthermore, a gradient coupling section is designed to effectively excite these plasmons and facilitate their transformation into high-purity vortex radiations. Experimentally, a plasmonic emitter is fabricated in the microwave region to validate the operational principle in terms of radiation patterns and the phase distributions of TCs. The proposed methodology fully exploits the OAM of the chiral plasmons and Brillouin-folding phenomena, boosting the development of compact and tunable generations of THz vortex beams.

2. RESULTS AND DISCUSSION

A. Chiral Plasmons Carrying OAMs

As illustrated in Fig. 1(a), the double-slots helical grating is employed here for achieving the compact and tunable vortex beam emitter since its eigenmodes are a series of chiral plasmons carrying OAMs. Therefore, the structural description and dispersion analysis are necessary for the following discussion and demonstration of the vorticity of these plasmons. The propagation and modulation periods of the helical periodic system are d and $L = 2d$, and the slot width is $a = d/2$. The outer radius of the helical grating is $R_1 = 3.5d$, whereas the inner radii of the two slots are $R_2 = R_3 = 2d$ for the uniform scheme. In the following, based on the multi-slots uniform helical grating, the general solution for its eigenmodes will be revealed to facilitate the understanding of the origin of the OAMs carried by chiral plasmons, where the cylindrical coordinate system is chosen for analysis. It is also supposed that all the field components are steady-state varying sinusoidally in time with monochromatic circular frequency ω, that is, time-harmonic fields. The helical grating used for the analysis contains G small slots of propagation period d within the modulation period L, thus $G = L/d$. Assuming the G slots have the same depth, the helical grating is thus uniform with a minimum period of d. For forward TM-polarized (electric field parallel to the z direction) modes existing in a right-handed periodic system, the $\mathbf{E}$ components should be Bloch states that can be labeled by the Bloch wave vector $\mathbf{k} = k_z\mathbf{b}_z$. Among them, k_z is the propagation constant lying in the Brillouin zone, and $\mathbf{b}_z = \hat{y}\,2\pi/d$ is the primitive reciprocal lattice vector. Thus, these eigenmodes are in the form [30]

$$\mathbf{E}_{k_z}(r,\varphi,z) = e^{jk_z z}\cdot\mathbf{u}_{k_z}(r,\varphi,z), \tag{1}$$

where (r,φ,z) are the coordinates in the cylindrical coordinate system, and $\mathbf{u}_{k_z}(r,\varphi,z)$ is a periodic function consistent with the periodicity of the helical system. According to the discrete translational symmetry along the z direction and the rotational symmetry around the z axis, the function $\mathbf{u}_{k_z}(r,\varphi,z)$ should satisfy the following periodic conditions:

$$\mathbf{u}_{k_z}(r,\varphi,z) = \mathbf{u}_{k_z}(r,\varphi,z+\kappa d), \qquad \kappa\in\mathbb{Z}, \tag{2}$$

$$\mathbf{u}_{k_z}(r,\varphi,z) = \mathbf{u}_{k_z}(r,\varphi+l\cdot 2\pi,z), \qquad l\in\mathbb{Z}. \tag{3}$$

In satisfying the periodic conditions above, the periodic function $\mathbf{u}_{k_z}(r,\varphi,z)$ relating to φ and z can be expanded into a double Fourier series of the form

$$\mathbf{u}_{k_z}(r,\varphi,z) = \mathbf{R}(r)\sum_{l=-\infty}^{\infty}\mathbf{A}_{\varphi}^{l}e^{jl\varphi}\sum_{\kappa=-\infty}^{\infty}\mathbf{A}_{z}^{\kappa}e^{-jk\frac{2\pi}{d}z}, \tag{4}$$

and the field expression Eq. (1) becomes

$$\mathbf{E}_{k_z}(r,\varphi,z) = \mathbf{R}(r)\sum_{l=-\infty}^{\infty}\mathbf{A}_{\varphi}^{l}e^{jl\varphi}\sum_{\kappa=-\infty}^{\infty}\mathbf{A}_{z}^{\kappa}e^{-j\left(k_z+\kappa\frac{2\pi}{d}\right)z}, \tag{5}$$

where $\mathbf{R}(r)$ is an eigenfunction of radial distance r, and $\mathbf{A}_{\varphi}^{l}$ and $\mathbf{A}_{z}^{\kappa}$ are the complex Fourier amplitudes of the electric field

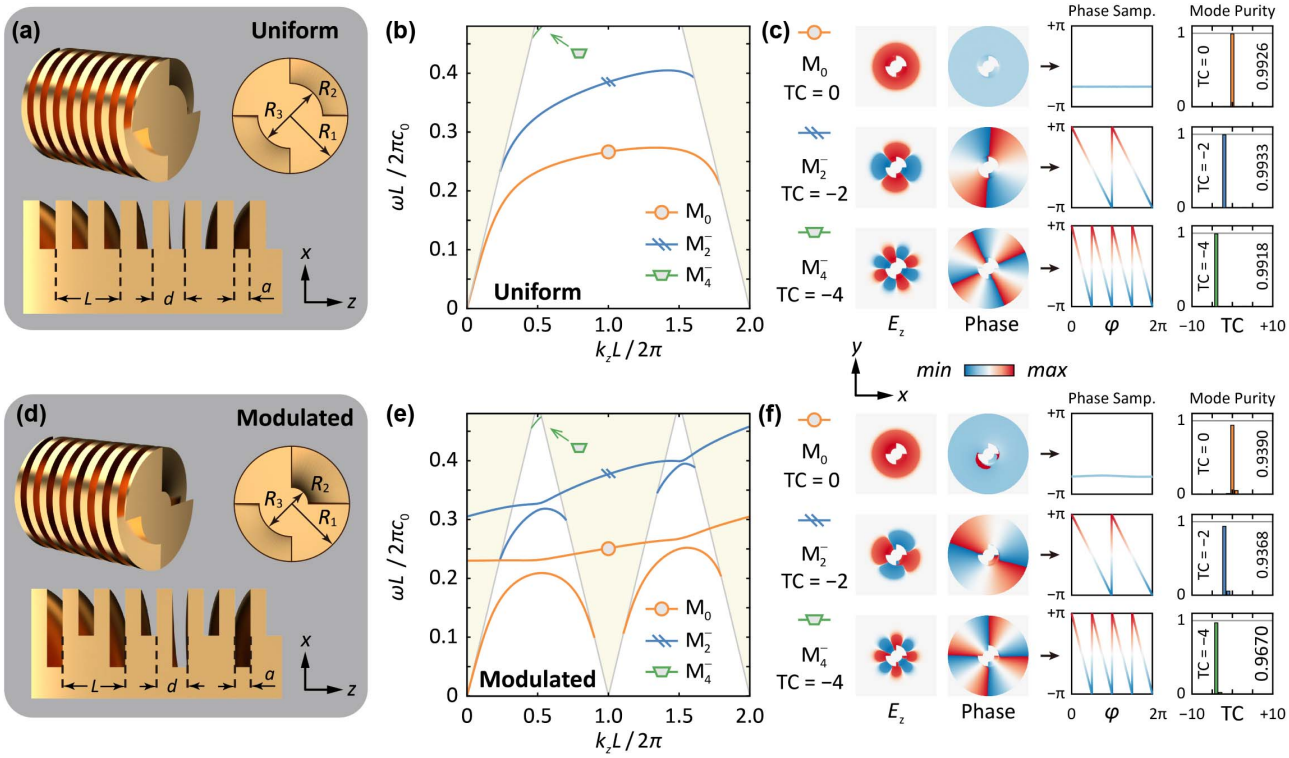

Fig. 1. Schematic diagram and dispersion analysis of double-slots helical grating with or without depth modulation. Panels (a), (b), and (c) present the structural descriptions, dispersion curves, and field distributions of eigenmodes for the uniform grating. On the other hand, panels (d), (e), and (f) depict the structural descriptions, dispersion curves, and field distributions of eigenmodes for the modulated grating.

associated with the azimuthal lth and axial κth space harmonics, and can be evaluated by

$$\mathbf{A}_{\varphi}^{l} \cdot \mathbf{A}_{z}^{\kappa} = \int_{0}^{2\pi} \int_{0}^{d} \frac{\mathbf{u}_{k_z}(r, \varphi, z)}{\mathbf{R}(r)} \, e^{-jl\varphi} e^{-jk\frac{2\pi}{d}z} \mathrm{d}\varphi \mathrm{d}z. \tag{6}$$

The initial coordinate is assumed to be (r_0, φ_0, z_0), where r_0 is the outer radius of the helical grating. When the eigenmode described by Eq. (5) propagates an arbitrary distance Δz along the z direction, to remain invariant, its azimuthal coordinate φ should also be rotated by an angle $\Delta\varphi$ satisfying

$$\Delta\varphi = \Delta z \frac{2\pi}{d \cdot G}, \tag{7}$$

where G is the number of slots in a period. This one-to-one correspondence is also requested inherently by the periodic helical structure. Hence, the periodic function at coordinates (r_0, φ_0, z_0) and $(r_0, \varphi_0 + \Delta\varphi, z_0 + \Delta z)$ should be identically described by the following relationship:

$$\begin{aligned} \mathbf{u}_{k_z}(r_0, \varphi_0, z_0) &= \mathbf{u}_{k_z}(r_0, \varphi_0 + \Delta\varphi, z_0 + \Delta z) \\ &= \mathbf{u}_{k_z}\left(r_0, \varphi_0 + \Delta z \frac{2\pi}{d \cdot G}, z_0 + \Delta z\right). \end{aligned} \tag{8}$$

Since the electric field has the form of Fourier series, the above equation becomes

$$\begin{aligned} &\mathbf{R}(r_0) \sum_{l=-\infty}^{\infty} \mathbf{A}_{\varphi_0}^{l} e^{jl\varphi_0} \sum_{\kappa=-\infty}^{\infty} \mathbf{A}_{z_0}^{\kappa} e^{-jk\frac{2\pi}{d}z_0} \\ &= \mathbf{R}(r_0) \sum_{l=-\infty}^{\infty} \mathbf{A}_{\varphi_0}^{l} e^{jl\varphi_0} \sum_{\kappa=-\infty}^{\infty} \mathbf{A}_{z_0}^{\kappa} e^{-jk\frac{2\pi}{d}z_0} \cdot e^{j\frac{2\pi}{d}\left(\frac{l}{G}-\kappa\right)\Delta z}. \end{aligned} \tag{9}$$

To ensure that the above equation is valid and physically achievable, the azimuthal and axial index of space harmonic should be identical, which gives

$$\begin{cases} \kappa = \frac{l}{G}, & \mathbf{A}_{\varphi_0}^{l} \neq 0, \quad \mathbf{A}_{z_0}^{\kappa} \neq 0 \\ \kappa \neq \frac{l}{G}, & \mathbf{A}_{\varphi_0}^{l} = 0, \quad \mathbf{A}_{z_0}^{\kappa} = 0 \end{cases}. \tag{10}$$

Hence, the electric field in Eq. (5) must be single Fourier series with $\kappa = l/G$:

$$\mathbf{E}_{k_z}(r, \varphi, z) = \sum_{m=-\infty}^{\infty} \mathbf{F}_{l}(r) e^{jl\varphi} e^{-j\left(k_z + \frac{l2\pi}{G\,d}\right)z}, \tag{11}$$

where the $\mathbf{F}_{l}(r) = \mathbf{A}_{\varphi}^{l} \cdot \mathbf{A}_{z}^{\kappa} \cdot \mathbf{R}(r)$ is a function that satisfies Helmholtz's equation in cylindrical coordinates. Hence, in the region of $r > r_0$, the function $\mathbf{F}_{l}(r)$ should be a series of modified Bessel function $K_{l}(\tau_{l} r)$, where $\tau_{l}^{2} = k^{2} - [k_z + 2\pi l/(Gd)]^{2}$ denotes the transverse angular wavenumber and $k = \omega(\mu_0 \varepsilon_0)^{(1/2)}$ is the wavenumber of the free space. By utilizing the method of Borgnis's potential, the E_z field components of the slow wave in the region of $r > r_0$ could be expressed as follows:

$$E_z = \sum_{l=-\infty}^{\infty} -\tau_l^2 \mathcal{A}_l K_l(\tau_l r) e^{jl\varphi} e^{-j\left(k_z + \frac{l2\pi}{Gd}\right)z}, \tag{12}$$

where $\mathcal{A}_l$ is the coefficient of the Fourier series of the scalar function utilized in the method of Borgnis's potential:

$$B_U = \sum_{l=-\infty}^{\infty} \mathcal{A}_l K_l(\tau_l r) e^{jl\varphi} e^{-j(k_z + \frac{l2\pi}{Gd})z}. \tag{13}$$

As described in Eq. (12), each eigenmode is characterized by the quantum number l, which is both the angular order and the longitudinal order of space harmonics. These eigenmodes represent space-sinusoidal waves, and their combination must satisfy the boundary condition of the helical grating. Interestingly, each mode exhibits a phase rotation factor $e^{jl\varphi}$, which corresponds to the rotational factor in the expressions of vortex beams. Thus, the lth-order mode carries OAM with a TC of l. When the dispersion relations of these space harmonics fall below the light line, chiral SSPs with TC $= l$ are formed. In particular, the analysis pertains to a right-handed helical system. In the case of a left-handed helical system, the OAM exhibits rotation in the opposite direction, i.e., TC $= -l$.

To validate the accuracy of the theoretical analysis, we employed the Eigenmode Solver in CST Studio Suite to calculate and analyze the dispersion and field distributions of the uniform double-slot helical grating, as illustrated in Figs. 1(b) and 1(c). Notably, the plasmonic modes showcased in this study exhibit positive group velocities and possess transverse even symmetry. This selection is based on the subsequent utilization of coaxial modes characterized by uniform field distributions in the transverse direction, which gradually transform into plasmonic modes. As this transformation occurs, the modes undergo equal compression within the two slots of the helical gratings. Consequently, only modes exhibiting even rotational symmetries in the transverse direction can be efficiently excited. This behavior is evident from the field distributions of plasmonic modes M_0, $M_{\bar{2}}$, and $M_{\bar{4}}$. For expression $M_m^{\pm}$, the lower and upper corners denote the absolute value of the TCs and the rotational direction of OAM. For mode M_0, the first row of Fig. 1(c) presents its E_z field and phase distributions. Its electric field exhibits an almost uniform distribution along the z axis, while the phase remains nearly constant. To verify the value and direction of the OAM carried by it, the normalized spectral weight or the so-called mode purity of the TC of mode M_0 is calculated by [31,32]

$$\mathcal{W}_m = \frac{\mathcal{P}_m}{\sum_{l=-\infty}^{\infty} \mathcal{P}_l}, \tag{14}$$

where $\mathcal{P}_m$ indicates the OAM spectrum weight of the spiral harmonic basis $e^{jm\varphi}$. To evaluate the mode purity, a circular curve, aligned with the helical grating, is employed as the sampling curve. Data points are uniformly placed along the sampling curve to capture the field properties accurately. In experimental measurements, both the amplitude and phase of the E_z field can be accurately measured, and these measurements can be conveniently converted to determine the real and imaginary parts of the field components. The mode purity can then be assessed using the discrete Fourier series provided by the following equation:

$$\mathcal{P}_l(\rho, z) = \frac{1}{N} \sum_{n=1}^{N} \mathcal{Q}(\rho, \varphi_n, z) e^{-jl\varphi_n}, \tag{15}$$

where N is the number of data points and $\mathcal{Q}(\rho, \varphi_n, z)$ is the complex quantity consisting of real and imaginary parts of the E_z field sampled on the sampling curve from the simulation:

$$\mathcal{Q}(\rho, \varphi_n, z) = \Re(E_z) + j\Im(E_z). \tag{16}$$

As illustrated in the first row of Fig. 1(c), the calculated mode purities based on Eq. (12) demonstrate that mode M_0 exhibits a high-purity OAM with a TC $= 0$, yielding a purity value of 0.9926. For mode $M_{\bar{2}}$, its field and phase distributions are illustrated in the second row of Fig. 1(c). When revolving around the z axis, the energy distribution remains nearly uniform, while the phase completes two full cycles from 0 to 2π. This behavior signifies its possession of OAM with a TC $= -2$, as corroborated by its mode purity of 0.9933. Likewise, for mode $M_{\bar{4}}$, its phase distribution is depicted in the third row of Fig. 1(c), revealing its association with OAM characterized by a TC $= -4$ and a remarkable purity of 0.9918. Thus, M_0, $M_{\bar{2}}$, and $M_{\bar{4}}$ correspond to chiral plasmons carrying high-purity OAM with TCs of 0, −2, and −4, respectively, aligning seamlessly with the theoretical predictions provided by Eq. (12). Under double-slots helical grating configuration, the E_z field of each dispersion line $\omega(m, k_z^0)$ shown in Fig. 1(b) with TC $= m$ in the region $0 < (L/2\pi) \cdot k_z^0 < 2$ can be expressed as

$$E^0_{z,(m,k_z^0)} = -\tau_m^2 \mathcal{A}_m K_m(\tau_m r) e^{jm\varphi} e^{-jk_z^0 z}, \quad m \in \mathbb{Z}, \quad 0 < \frac{L}{2\pi} \cdot k_z^0 < 2, \tag{17}$$

which is a simplified form of the general solution of Eq. (12), and can be utilized to describe the vortex characteristics of the supported chiral plasmons of the helical grating. In the following, we will focus only on the dispersion lines within $0 < (L/2\pi) \cdot k_z^0 < 2$. As depicted in Fig. 1(b), this is the smallest region within the momentum space for which the dispersion $\omega(m, k_z^0)$ possesses the full characteristics of the helical periodic system owing to translational symmetry. In addition, according to the periodic conditions Eqs. (2), (3), and (7), the total dispersion relation $\omega(l, k_z)$ over the momentum space should also be periodic in k_z and l, thereby satisfying the following condition:

$$\omega(l, k_z) = \omega\left(l + \mathcal{N} \cdot G, k_z + \mathcal{N}\frac{2\pi}{d}\right) = \omega\left(l + \mathcal{N} \cdot G, k_z + \mathcal{N} \cdot G \cdot \frac{2\pi}{L}\right), \tag{18}$$

where $\mathcal{N} \in \mathbb{Z}$. Since G equals 2 in the proposed M_0 double-slots system, the above equation should take the following form:

$$\omega\left(l + 2\mathcal{N}, k_z + 2\mathcal{N} \cdot \frac{2\pi}{L}\right) = \omega(l, k_z). \tag{19}$$

Accordingly, the E_z field of an arbitrary mode $M^{\pm}_{|m+2\mathcal{N}|}$ within $2\mathcal{N} < (L/2\pi) \cdot k_z^{2\mathcal{N}} < 2(\mathcal{N}+1)$ can be expressed by the following transformation of Eq. (17) according to Eq. (19):

$$E^{2\mathcal{N}}_{z,(m,k_z^{2\mathcal{N}})} = -\tau_m^2 \mathcal{A}_m K_m(\tau_m r) e^{jl\varphi} e^{-jk_z^{2\mathcal{N}} z},$$
$$2\mathcal{N} < \frac{L}{2\pi} \cdot k_z^{2\mathcal{N}} < 2(\mathcal{N}+1), \tag{20}$$

where $l = m + 2\mathcal{N}$ is defined as the integrated TC of the dispersion line for its corresponding Brillouin region.

For the uniform grating, it can be observed from Fig. 1(b) that the dispersion curves of the supported chiral plasmons lie below the light cone and their wave vectors exceed those of free space. Consequently, these plasmons are tightly confined to the surface of the grating. To facilitate their diffraction into free space and the generation of vortex beams, a scheme employing modulation of the grating slot depth is adopted. This approach harnesses the Brillouin-zone folding phenomenon, compensating for the wave vector mismatch between these modes and the free-space modes. By exploiting band folding, the discrepancy in wave vectors is remedied, allowing for efficient diffraction of the excited chiral plasmons into vortex wave beams. Figure 1(d) presents the structural schematic of the modulation scheme, where one slot is deeper than the other, as indicated by $R_2 = 0.9R_3$. The field and phase distributions of modes M_0, M_2^-, and M_4^-, computed using the CST Eigenmode Solver, are shown in Fig. 1(f). These distributions confirm that these modes are chiral plasmons carrying OAMs with TCs of 0, −2, and −4, respectively. The dispersion curves of the modulated scheme obtained through eigenmode analysis are presented in Fig. 1(e). Compared to the uniform one, these curves fold back within the boundaries of the Brillouin zone, falling into the fast-wave region (yellow shaded region). Consequently, when excited, these chiral plasmons within the fast-wave region undergo diffraction with the −1st spatial harmonic, resulting in the generation of free-space vortex beams. According to Eq. (17) and Bloch's theorem, the diffraction wave of the mth mode $M_{|m|}^{+(-)}$ within $0 < (L/2\pi) \cdot k_z^0 < 2$ can be written in the following general form:

$$E^0_{z,(m,k_z^0)} = -\tau_m^2 \mathcal{A}_m K_m(\tau_m r) e^{jm\varphi} e^{-jk_z^0 z} \cdot \mathcal{Z}(\varphi, z),$$
$$0 < \frac{L}{2\pi} \cdot k_z^0 < 2, \tag{21}$$

where $\mathcal{Z}(\varphi, z)$ is a periodic function with the same periodicity as the modulated grating. Therefore, the following three periodic conditions hold:

$$\begin{cases} \mathcal{Z}(\varphi, z) = \mathcal{Z}(\varphi, z + n \cdot L), & n \in Z, \\ \mathcal{Z}(\varphi, z) = \mathcal{Z}(\varphi + n \cdot 2\pi, z), \\ \mathcal{Z}(\varphi, z) = \mathcal{Z}(\varphi + \Delta\varphi, z + \Delta z) = \mathcal{Z}\left(\varphi + \Delta z \frac{2\pi}{L}, z + \Delta z\right), \end{cases} \tag{22}$$

where the distance Δz and the angle $\Delta\varphi$ should satisfy $\Delta\varphi = 2\pi\Delta z/L$. Similar to the analysis method for $\mathbf{u}_{k_z}(r, \varphi, z)$ relating to Eqs. (4) to (10), $\mathcal{Z}(\varphi, z)$ can be expressed as a Fourier series of k_z:

$$\mathcal{Z}(\varphi, z) = \sum_{n=-\infty}^{\infty} \mathcal{B}_n e^{jn\varphi} e^{-jn\frac{2\pi}{L}z}, \tag{23}$$

where n is the diffraction order of the space harmonic belonging to the modulated helical system, and the coefficient $\mathcal{B}_n$ can be calculated by

$$\mathcal{B}_n = \int_0^{2\pi} \int_0^L \mathcal{Z}(\varphi, z) e^{-jn\varphi} e^{-jn\frac{2\pi}{d}z} \mathrm{d}\varphi \mathrm{d}z. \tag{24}$$

Therefore, the fundamental general form Eq. (21) of the mode within $0 < (L/2\pi) \cdot k_z^0 < 2$ becomes

$$E^0_{z,(m,n,k_z^0)} = \sum_{n=-\infty}^{\infty} -\tau_m^2 \mathcal{A}_m \mathcal{B}_n K_m(\tau_m r) e^{jl\varphi} e^{-jk_z^n z},$$
$$n < \frac{L}{2\pi} \cdot k_z^n < n + 2, \tag{25}$$

where l indicates the integrated TC carried by the nth-order diffraction of modes $M_{|m|}^{\pm}$ within $0 < (L/2\pi) \cdot k_z^0 < 2$,

$$l = m + n. \tag{26}$$

Then, the E_z field of an arbitrary mode $M_{|m+\mathcal{N}|}^{\pm}$ within $\mathcal{N} < (L/2\pi) \cdot k_z^{\mathcal{N}} < \mathcal{N} + 1$ can be obtained by

$$E^{\mathcal{N}}_{z,(m,n,k_z^{\mathcal{N}})} = \sum_{n=-\infty}^{\infty} -\tau_m^2 \mathcal{A}_m \mathcal{B}_n K_m(\tau_m r) e^{jl\varphi} e^{-jk_z^{n+\mathcal{N}} z},$$
$$n + \mathcal{N} < \frac{L}{2\pi} \cdot k_z^{n+\mathcal{N}} < n + \mathcal{N} + 2, \tag{27}$$

where l indicates the integrated TC carried by the nth-order diffraction of modes $M_{|m+\mathcal{N}|}^{\pm}$ within $\mathcal{N} < (L/2\pi) \cdot k_z^{\mathcal{N}} < \mathcal{N} + 1$,

$$l = m + n + \mathcal{N}, \tag{28}$$

thereby enabling additive (subtractive) manipulation of the TC through diffraction. In addition to this, the nth-order diffraction of $M_{|m+\mathcal{N}|}^{\pm}$ also superimposes the propagation constants $k_z^{\mathcal{N}}$ with $n2\pi/L$, i.e., $k_z^{n+N} = k_z^0 + (n + \mathcal{N})2\pi/L$. This is the key to achieving wave vector compensation between the chiral plasmons and free-space vortex beams, thus converting the modes $M_{|m+\mathcal{N}|}^{\pm}$ into vortex beams. Regarding Eq. (27), the compensation requires the relation $-1 < (L/2\pi) \cdot k_z^{n+\mathcal{N}} < +1$ to be established, i.e., $n + \mathcal{N} = -1$. Hence, for arbitrary SSP $M_{|m|}^{\pm}$, the ultimate TC of the vortex beam by its diffraction is

$$l = m - 1. \tag{29}$$

Based on the above discussion, the $-(1 + \mathcal{N})$th-order diffraction of an arbitrary mode $M_{|m+\mathcal{N}|}^{\pm}$ within $\mathcal{N} < (L/2\pi) \cdot k_z^{\mathcal{N}} < \mathcal{N} + 1$ yields the vortex beam with integrated TC $= m - 1$. Since the intensity of the fundamental space harmonics is the highest, only the diffraction characteristics of the SSPs $M_{|m|}^{\pm}$ within $0 < (L/2\pi) \cdot k_z^0 < 2$ will be discussed in the following. For the sake of meeting the compensation condition, the diffraction order should be $n = -1$, and Eq. (25) becomes

$$E^0_{z,(m,-1,k_z^0)} = \sum_{n=-\infty}^{\infty} -\tau_m^2 \mathcal{A}_m \mathcal{B}_n K_m(\tau_m r) e^{j(m-1)\varphi} e^{-jk_z^{-1} z},$$
$$-1 < \frac{L}{2\pi} \cdot k_z^{-1} < +1. \tag{30}$$

It can be confirmed that the propagation constant k_z^0 decreases by $2\pi/L$ from Eq. (30). Therefore, as the modes within the light cone undergo −1st-order diffraction, their wave vectors remain confined within the light cone. This wavenumber compensation process enables the direct transformation of these chiral plasmons into vortex beams. Therefore, with the

introduction of depth modulation in the helical grating, the modes M_0, M_2^-, and M_4^- carrying TCs of 0, −2, and −4, respectively, undergo diffraction and transform into vortex beams with TCs of −1, −3, and −5 according to the ultimate TC indicated by Eq. (29).

B. Excitation of Chiral Plasmons and Generation of Vortex Beams

To efficiently excite these chiral plasmons and validate their conversion into vortex radiation, a coupler is designed as shown in Fig. 2(a). Based on a gradient grating and a carefully designed outer conductor structure, this coupler enables the transformation of coaxial modes into plasmons carrying OAMs. The coupling section consists of an inner conductor with gradually increasing grating depth and an outer conductor with contour lines gradually moving away from the grating. The total length along the z direction of the coupling section is $G = 8d$, corresponding to eight transmission periods. As the grating depth of the inner conductor gradually increases from 0 to h, the contour lines of the outer conductor move away from the inner conductor according to the equation $y = C_1 e^{\alpha z} + C_2\,(z_1 < z < z_2)$, gradually converting coaxial modes into plasmonic modes on the helical grating, where $C_1 = (y_2 - y_1)/(e^{\alpha z_2} - e^{\alpha z_1})$, $C_2 = (y_1 e^{\alpha z_2} - y_2 e^{\alpha z_1})/(e^{\alpha z_2} - e^{\alpha z_1})$, and $\alpha = 0.04$. To illustrate the working principle of the coupling section more clearly, the dispersion of mode M_0 as a function of grating depth, with a spacing of $0.17h$, is shown in Fig. 2(b). When the grating depth is 0, the dispersion of the mode M_0 coincides with that of the coaxial mode, perfectly matching the dispersion curve of the light. As the depth of the gradient grating gradually increases, the dispersion curve of the mode M_0 gradually splits from the light line, with an increasing wave vector in the longitudinal direction, exhibiting the characteristics of near-field localization of slow-wave modes. Therefore, based on the depth-gradient grating, the mismatched wave vectors can be gradually compensated, allowing for an effective transformation of coaxial modes into plasmonic modes. To validate the performance of the designed coupler, the field distribution of the system at the normalized frequency $f_{\text{norm}} = 0.24$ is also presented in Fig. 2(c). It can be observed that the coaxial mode excited at Port 1 gradually converts into the mode M_0 on the grating with the assistance of the coupler. As the plasmonic waves crawl over the grating surface and reach another coupler, the mode M_0 is efficiently converted back into the coaxial mode based on the reciprocity principle and transmitted to Port 2. Apart from mode M_0, similar analysis can be applied to modes M_2^- and M_4^-, which can also be effectively excited from coaxial modes with the assistance of the coupler.

To further validate the excitation effectiveness, a sampling line is introduced along the propagation direction on the grating surface to examine their spatial distribution in the wavenumber domain, as shown by the red dashed line in Fig. 3(a). This sampling line allowed us to capture the spatial distribution of the excited modes at different frequencies. Subsequently, a one-dimensional spatial Fourier transform is performed on the field distribution at each frequency, resulting in the wavenumber distribution of the excited modes, represented by the red circles in Fig. 3(b). Upon analysis, it is observed that as the frequency increases, the wavenumber distribution of the excited modes closely matches the dispersion curve of the grating. This alignment indicated an effective transformation of the coaxial modes into modes M_0, M_2^-, and M_4^-, which can be further supported by the excellent transmission characteristics from Port 1 to Port 2, as depicted in Fig. 3(c). However, it is important to note the presence of a photonic bandgap (PBG) between the dispersion curves of modes M_2^- and M_4^-. The frequency range of this bandgap, marked by the red shaded region in Fig. 3(b), indicated that the grating does not support the propagation of modes within this range. As a result, the transmission performance experienced a decline in this frequency range, as demonstrated in Fig. 3(c). Consequently, when the coaxial mode is output from the coupler, it cannot be converted into plasmons propagating along the grating surface within the PBG. Instead, it directly generates vortex radiation propagating toward free space, carrying OAM akin to its corresponding mode. Figure 3(b) reveals that the wavenumber distribution of the field detected within the PBG is almost an extension of the dispersion curve of mode M_4^- in the fast-wave region. Hence, this mode can be considered a variant of mode M_4^- within the outer conductor and helical grating system, exhibiting similar transverse field distribution and carrying the same OAM as mode 4. Consequently, the vortex radiation generated within the PBG carries a TC = −4.

Then, the depth modulation scheme is introduced to convert the excited plasmons carrying OAMs into vortex radiation, as illustrated in Fig. 3(d). Building upon the theoretical analysis presented earlier, the effectiveness of this excitation method is further validated by examining the wavenumber distribution of the field excited on the modulated grating surface at different frequencies, as depicted by the red circles in Fig. 3(e).

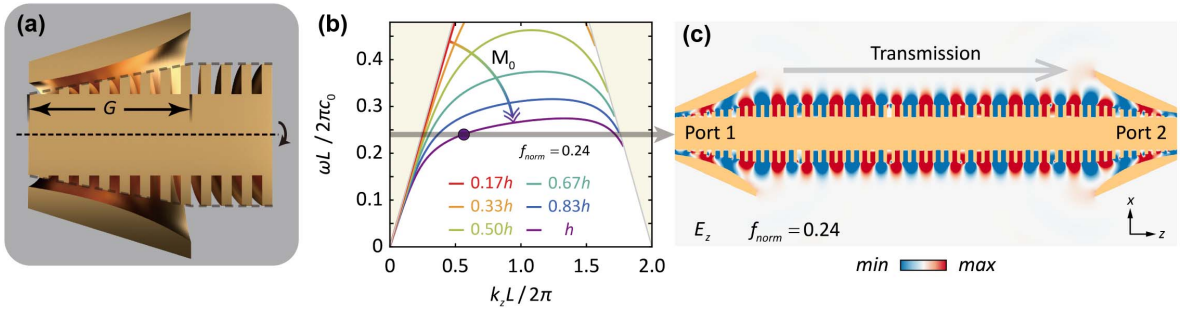

Fig. 2. Excitation of the chiral plasmons. (a) Coupler utilized for the transformation of coaxial modes into plasmonic modes. (b) Dispersion curves of mode M_0 as the slot depth increases. (c) Field distribution of plasmonic transmission.

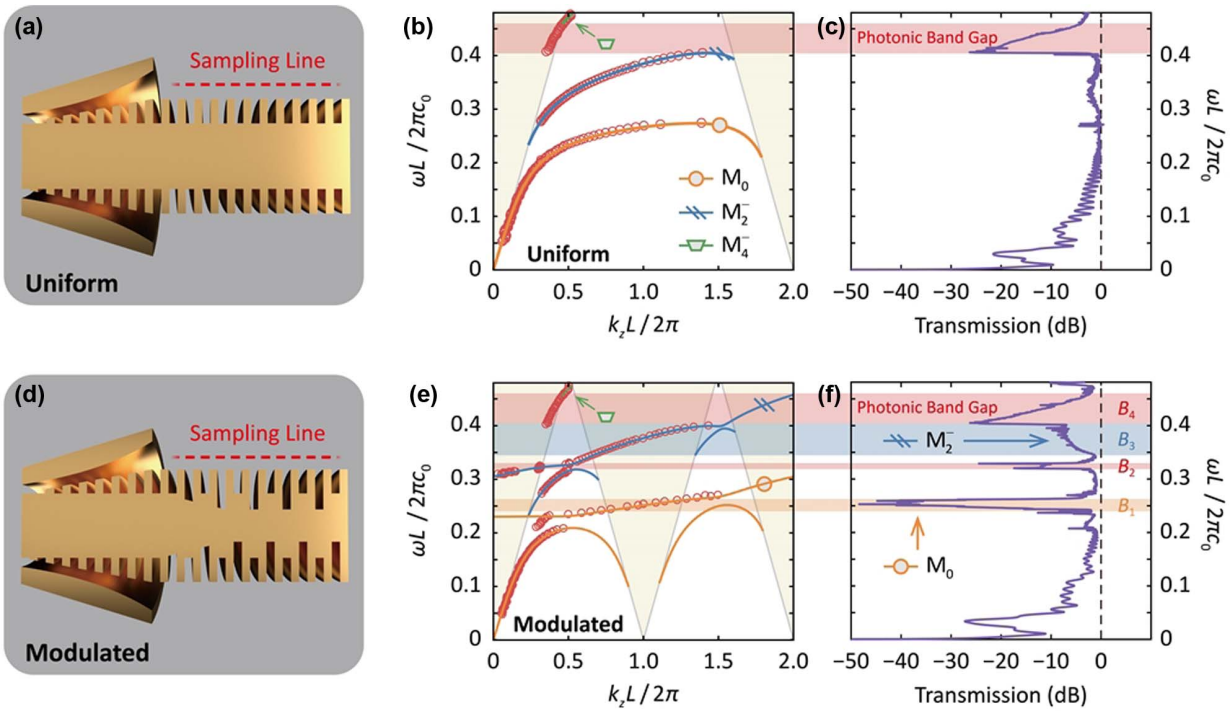

Fig. 3. Verification of the excitation of the chiral plasmons. Panels (a), (b), and (c) show the schematic diagrams, sampling results, and transmission characteristics of the uniform grating, while panels (d), (e), and (f) depict the schematic diagrams, sampling results, and transmission characteristics of the modulated grating.

Remarkably, the distribution of the excited field in momentum space is closely aligned with the dispersion curves of the eigenmodes supported by the modulated grating, thereby substantiating the efficacy of this excitation approach. In comparison to the uniform grating, the presence of Brillouin zone folding led to a partial overlap between the dispersion curves of modes M_2^- and M_4^- with the fast-wave region, as evidenced by the orange and blue shaded regions in Fig. 3(e). These regions are identified as bands B_1 and B_3, respectively. Consequently, the modes M_2^- and M_4^- within the bands B_1 and B_3 undergo −1st-order diffraction, resulting in their conversion into vortex radiation propagating toward free space. Specifically, the vortex beam from mode M_2^- acquired a TC = −1, while the other one exhibited a TC = −3. These findings highlight the transformation of coaxial modes into chiral plasmons through the interaction with the modulated grating. In addition to these discovered radiation bands, two additional bands labeled as bands B_2 and B_4 emerged due to the emergence of the PBG, as indicated by the red shaded regions in Fig. 3(e). Band B_4, formed within the frequency interval created by the PBG between modes M_2^- and M_4^-, exhibited a transverse field distribution similar to that of mode M_4^-. However, owing to its compatibility with free-space wave vectors, the waves within the band B_4 directly transformed into vortex radiation carrying an OAM with TC = −4. Similarly, band B_2 originated from the PBG within the slow-wave region resulting from the splitting band of the mode M_2^-. The transverse field distribution of the converted coaxial modes within this frequency range resembled mode M_2^-, enabling their direct transformation into vortex radiation with the OAM TC of −2, thanks to their wave vector matching with free space. Consequently, the depth-modulated helical system facilitated the simultaneous generation of vortex beams carrying TCs of −1, −2, −3, and −4 within the frequency intervals of radiation bands B_1, B_2, B_3, and B_4, respectively. The radiation characteristics of these bands are further corroborated through the analysis of the transmission properties depicted in Fig. 3(f). As anticipated, the presence of −1st-order diffraction and the PBG resulted in a reduction in the transmission performance within the frequency intervals of radiation bands B_1, B_2, B_3, and B_4, aligning with the simulated transmission characteristics and confirming the successful conversion and transmission of chiral plasmons in the system.

To further confirm the validity of the aforementioned analysis, we perform simulations at normalized frequencies 0.2587, 0.3227, 0.3941, and 0.4203 within the bands B_1, B_2, B_3, and B_4, respectively. These calculations focus on evaluating the distribution of the radiation field, phase distribution, far-field directivity, and mode purity associated with the OAMs carried by the beams. The results, illustrated in Fig. 4, unequivocally demonstrate the generation of vortex beams with distinct TCs of −1, −2, −3, and −4, respectively. The vortex radiation within bands B_1 and B_3 results from the −1st-order spiral diffraction of modes M_0 and M_2^-, transforming into vortex beams propagating in free space. According to Eq. (1), their expected TCs are −1 and −3, which harmoniously align with the results obtained from the simulation analysis in Figs. 4(a) and 4(c). Additionally, their mode purities are determined to be 0.934 and 0.768, respectively. In contrast, the vortex radiations within bands B_2 and B_4 are directly generated from the fast-wave modes with transverse distributions resembling

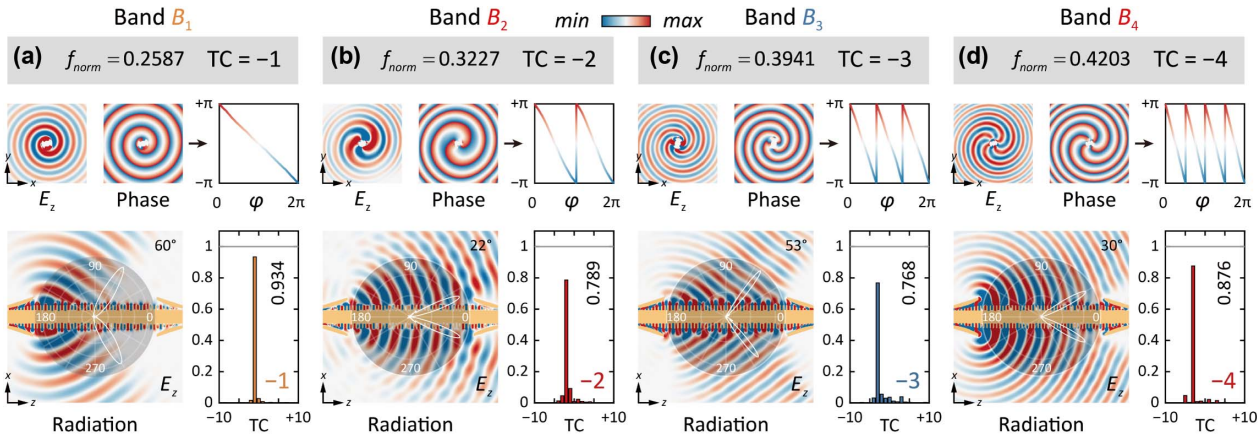

Fig. 4. Generation of the vortex beams. (a), (b), (c), and (d) are radiation field distributions, far-field directivities, and mode purities of generated vortex beams in bands B_1, B_2, B_3, and B_4.

modes M_2^- and M_4^-. Hence, their TCs are expected to be −2 and −4, respectively, in agreement with the results of the simulation analysis in Figs. 4(b) and 4(d). Their corresponding mode purities are evaluated as 0.789 and 0.876, respectively. Thus, the depth-modulated scheme enables the simultaneous generation of vortex beams with TCs ranging from −1 to −4 within the four radiation bands. This achievement not only validates the effectiveness of depth modulation for controlled vortex plasmon emission but also underscores its potential for various applications.

3. EXPERIMENTAL VERIFICATION

To experimentally validate the working principle, we fabricate the plasmonic vortex beam emitter in the microwave band, as shown in Fig. 5(d). The helical grating is first printed out with the whole frame by aluminum alloy AlSi10Mg through a commercial three-dimensional printing technique and then coated with copper by the electroplating process. The structural parameters suitable for the microwave band are as follows: $d = 3.60$ mm, $L = 7.20$ mm, $a = 1.80$ mm, $R_1 = 12.60$ mm, $R_2 = 7.20$ mm, and $R_3 = 6.48$ mm. It is noteworthy that

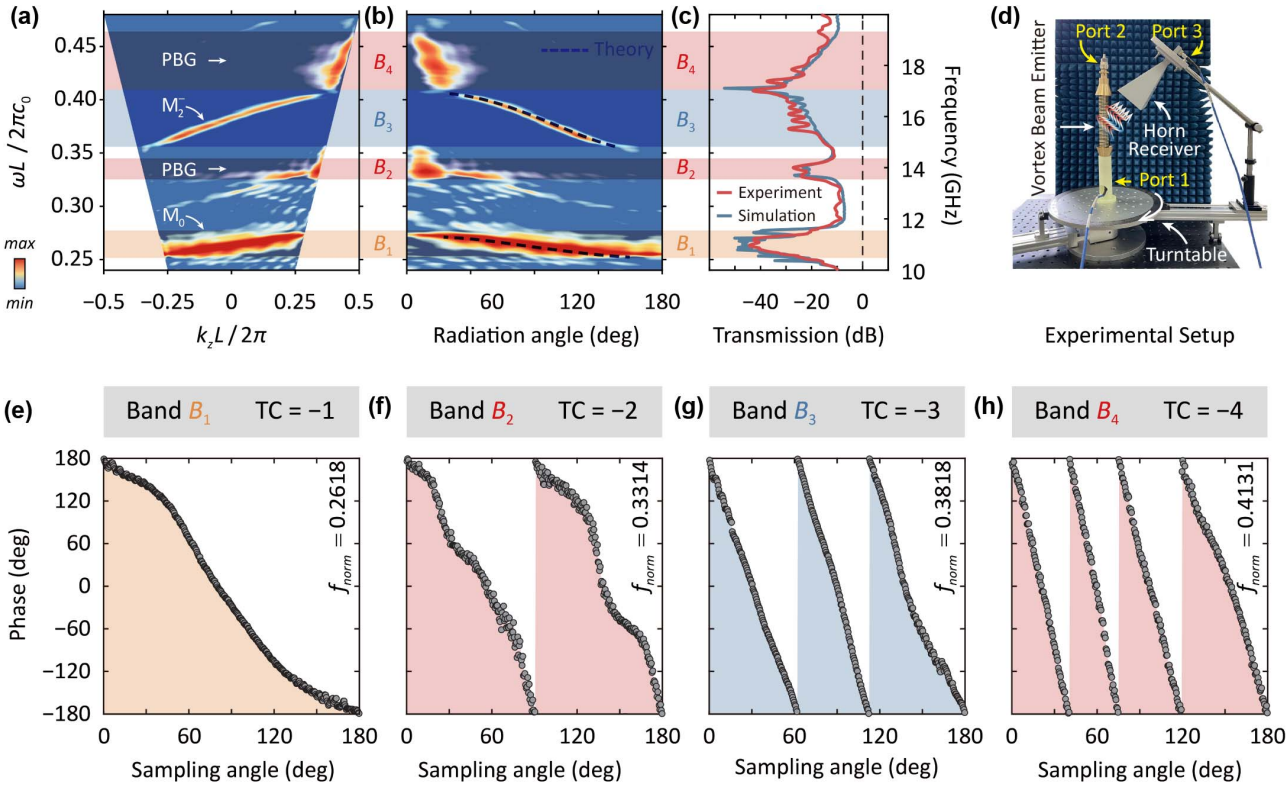

Fig. 5. Experimental setups and measured results. (a) Measured dispersion of the radiation waves from the vortex beam emitter. (b) Measured and theoretical beam scanning characteristics. (c) Measured and simulated transmission performances between two couplers. (d) Experimental setups. (e), (f), (g), and (h) are phase distributions of generated vortex beams in bands B_1, B_2, B_3, and B_4.

the actual manufactured helical grating has increased in size after being coated with copper, and the measured outer radius R_1 is 12.62 mm instead of 12.60 mm. Thus, the machining error is approximately 0.1587%, which is within an acceptable range. The overall experimental setups for the vortex beam antenna are presented in Fig. 5(d), comprising an Agilent N5245A PNA-X network analyzer (10 MHz to 50 GHz), a high-gain horn antenna for receiving the vortex radiation signal, a turntable for signal reception from different directions, a computer for programming the vector network analyzer (VNA), and the fabricated vortex emitter. During the tests, the vortex beam emitter is connected to the VNA through an N-type connector and powered through the SubMiniature version A (SMA) port. Port 1 and Port 2 of the VNA are connected to the couplers of the plasmonic emitter, while Port 3 is connected to the horn antenna for measuring far-field radiation performance. Figure 5(c) presents the transmission characteristics at both ends of the vortex beam emitter obtained from experimental testing and simulations accounting for losses, marked by blue and red lines, respectively. The simulation results exhibit good agreement with the experimental measurements, showing a consistent decrease in transmission characteristics across bands B_1, B_2, B_3, and B_4, as predicted by the theoretical analysis. Waves that do not transmit through the grating are transformed into free-space vortex beams, which are detected by the horn antenna in the far field, as confirmed by the measured dispersion and beam-scanning characteristics shown in Figs. 5(a) and 5(b).

Within bands B_1 and B_3, the vortex radiation results from the −1st-order diffraction of modes M_0 and M_2^-, giving rise to wide-angle beam scanning characteristics. As the frequency decreases, the radiation direction increases from 30° to 150°. The phase distributions at frequencies 0.2618 and 0.3818 within these bands are shown in Figs. 5(e) and 5(g), respectively. As the detection horn rotates a full circle, the phase of the longitudinal electric field at these frequencies decreases by 1 and 3 times, respectively, confirming their TCs of −1 and −3. In addition to these two bands, two radiation spectra are observed within the 0° to 30° radiation range, as depicted in Fig. 5(b). These spectra correspond to the PBG bands B_2 and B_4, whose waves are directly radiated out of the coupler without beam scanning capability. The phase distributions at frequencies 0.3314 and 0.4131 within these bands are shown in Figs. 5(f) and 5(h), respectively, decreasing by 2 and 4 times from 0 to 2π as the horn rotates, confirming their TCs of −2 and −4. Thus, through the spectral and phase distributions of the radiation waves, we have demonstrated that the designed vortex beam emitter can simultaneously generate vortex radiation with TCs ranging from −1 to −4.

4. CONCLUSION

In conclusion, we present a theoretical proposal and experimental demonstration of a chiral plasmons-enabled vortex beam emitter, capable of simultaneously generating multi-mode and highly pure vortex beams separate in multiple narrow bands. By incorporating depth modulation into the helical periodic system, the eigenmodes carrying OAMs undergo alternating transformations into vortex radiations, following the principles of the Bragg law. Through experimental observations of the measured radiation patterns and phase distributions, our designed plasmonic vortex beam emitter convincingly exhibits the generation of vortex beams with TCs of −1, −2, −3, and −4. This proposed scheme offers a promising avenue for the generation of multi-mode, tunable, and high-purity vortex beams in the THz frequency range, paving the way for advanced OAM-based communication and spectroscopy.

Funding. National Natural Science Foundation of China (62271011, U21A20458); National Key Research and Development Program of China (2021YFA1600302); Beijing Science Foundation for Distinguished Young Scholars (JQ21011).

Acknowledgment. The authors acknowledge discussions with Fan-Hong Li.

Disclosures. The authors declare no competing interests.

Data Availability. The data that support the findings of this study are available from the corresponding author upon reasonable request.

REFERENCES

1. L. Allen, M. W. Beijersbergen, R. J. C. Spreeuw, and J. P. Woerdman, "Orbital angular momentum of light and the transformation of Laguerre-Gaussian laser modes," Phys. Rev. A **45**, 8185–8189 (1992).
2. G. Indebetouw, "Optical vortices and their propagation," J. Mod. Opt. **40**, 73–87 (1993).
3. Y. Shen, X. Wang, Z. Xie, C. Min, X. Fu, Q. Liu, M. Gong, and X. Yuan, "Optical vortices 30 years on: OAM manipulation from topological charge to multiple singularities," Light Sci. Appl. **8**, 90 (2019).
4. M. Padgett and R. Bowman, "Tweezers with a twist," Nat. Photonics **5**, 343–348 (2011).
5. A. E. Willner, H. Huang, Y. Yan, Y. Ren, N. Ahmed, G. Xie, C. Bao, L. Li, Y. Cao, Z. Zhao, J. Wang, M. P. J. Lavery, M. Tur, S. Ramachandran, A. F. Molisch, N. Ashrafi, and S. Ashrafi, "Optical communications using orbital angular momentum beams," Adv. Opt. Photonics **7**, 66–106 (2015).
6. A. Sit, F. Bouchard, R. Fickler, J. Gagnon-Bischoff, H. Larocque, K. Heshami, D. Elser, C. Peuntinger, K. Günthner, B. Heim, C. Marquardt, G. Leuchs, R. W. Boyd, and E. Karimi, "High-dimensional intracity quantum cryptography with structured photons," Optica **4**, 1006–1010 (2017).
7. J. Vieira, R. M. G. M. Trines, E. P. Alves, R. A. Fonseca, J. T. Mendonça, R. Bingham, P. Norreys, and L. O. Silva, "Amplification and generation of ultra-intense twisted laser pulses via stimulated Raman scattering," Nat. Commun. **7**, 10371 (2016).
8. H. Zhou, X. Su, A. Minoofar, R. Zhang, K. Zou, H. Song, K. Pang, H. Song, N. Hu, Z. Zhao, A. Almaiman, S. Zach, M. Tur, A. F. Molisch, H. Sasaki, D. Lee, and A. E. Willner, "Utilizing multiplexing of structured THz beams carrying orbital-angular-momentum for high-capacity communications," Opt. Express **30**, 25418–25432 (2022).
9. A. A. Sirenko, P. Marsik, C. Bernhard, T. N. Stanislavchuk, V. Kiryukhin, and S. W. Cheong, "Terahertz vortex beam as a spectroscopic probe of magnetic excitations," Phys. Rev. Lett. **122**, 237401 (2019).
10. K. Miyamoto, K. Suizu, T. Akiba, and T. Omatsu, "Direct observation of the topological charge of a terahertz vortex beam generated by a Tsurupica spiral phase plate," Appl. Phys. Lett. **104**, 261104 (2014).
11. Z. Xie, X. Wang, J. Ye, S. Feng, W. Sun, T. Akalin, and Y. Zhang, "Spatial terahertz modulator," Sci. Rep. **3**, 3347 (2013).

12. J. He, X. Wang, D. Hu, J. Ye, S. Feng, Q. Kan, and Y. Zhang, "Generation and evolution of the terahertz vortex beam," Opt. Express **21**, 20230–20239 (2013).
13. B. A. Knyazev, Y. Y. Choporova, M. S. Mitkov, V. S. Pavelyev, and B. O. Volodkin, "Generation of terahertz surface plasmon polaritons using nondiffractive Bessel beams with orbital angular momentum," Phys. Rev. Lett. **115**, 163901 (2015).
14. B. Volodkin, Y. Choporova, B. Knyazev, G. Kulipanov, V. Pavelyev, V. Soifer, and N. Vinokurov, "Fabrication and characterization of diffractive phase plates for forming high-power terahertz vortex beams using free electron laser radiation," Opt. Quantum Electron. **48**, 223 (2016).
15. R. Imai, N. Kanda, T. Higuchi, K. Konishi, and M. Kuwata-Gonokami, "Generation of broadband terahertz vortex beams," Opt. Lett. **39**, 3714–3717 (2014).
16. J. B. Pendry, L. Martín-Moreno, and F. J. Garcia-Vidal, "Mimicking surface plasmons with structured surfaces," Science **305**, 847–848 (2004).
17. Z. Gao, L. Wu, F. Gao, Y. Luo, and B. Zhang, "Spoof plasmonics: from metamaterial concept to topological description," Adv. Mater. **30**, 1706683 (2018).
18. L. Tong, H. Wei, S. Zhang, and H. Xu, "Recent advances in plasmonic sensors," Sensors **14**, 7959–7973 (2014).
19. S. Roh, T. Chung, and B. Lee, "Overview of the characteristics of micro- and nano-structured surface plasmon resonance sensors," Sensors **11**, 1565–1588 (2011).
20. L. Liu, Z. Han, and S. He, "Novel surface plasmon waveguide for high integration," Opt. Express **13**, 6645–6650 (2005).
21. L. Yin, V. K. Vlasko-Vlasov, J. Pearson, J. M. Hiller, J. Hua, U. Welp, D. E. Brown, and C. W. Kimball, "Subwavelength focusing and guiding of surface plasmons," Nano Lett. **5**, 1399–1402 (2005).
22. Z. Liu, H. Lee, Y. Xiong, C. Sun, and X. Zhang, "Far-field optical hyperlens magnifying sub-diffraction-limited objects," Science **315**, 1686 (2007).
23. F. J. Garcia-Vidal, A. I. Fernández-Domínguez, L. Martin-Moreno, H. C. Zhang, W. Tang, R. Peng, and T. J. Cui, "Spoof surface plasmon photonics," Rev. Mod. Phys. **94**, 025004 (2022).
24. C. R. Williams, S. R. Andrews, S. A. Maier, A. I. Fernández-Domínguez, L. Martín-Moreno, and F. J. García-Vidal, "Highly confined guiding of terahertz surface plasmon polaritons on structured metal surfaces," Nat. Photonics **2**, 175–179 (2008).
25. F. Rüting, A. I. Fernández-Domínguez, L. Martín-Moreno, and F. J. García-Vidal, "Subwavelength chiral surface plasmons that carry tuneable orbital angular momentum," Phys. Rev. B **86**, 075437 (2012).
26. J.-F. Zhu, C.-H. Du, Z.-W. Zhang, and F.-H. Li, "Generating a multimode vortex beam based on spoof surface plasmon polaritons," Opt. Lett. **47**, 4459–4462 (2022).
27. A. Bera, R. K. Barik, M. Sattorov, O. Kwon, S.-H. Min, I.-K. Baek, S. Kim, J.-K. So, and G.-S. Park, "Surface-coupling of Cerenkov radiation from a modified metallic metamaterial slab via Brillouin-band folding," Opt. Express **22**, 3039–3044 (2014).
28. J. F. Zhu, C. H. Du, F. H. Li, L. Y. Bao, and P. K. Liu, "Free-electron-driven multi-frequency terahertz radiation on a super-grating structure," IEEE Access **7**, 181184 (2019).
29. Z.-W. Zhang, J.-F. Zhu, C.-H. Du, F. Gao, F.-Y. Han, and P.-K. Liu, "Chiral plasmons enable coherent vortex Smith–Purcell radiation," Laser Photonics Rev. **17**, 2200420 (2023).
30. K. Zhang, D. Li, K. Chang, K. Zhang, and D. Li, *Electromagnetic Theory for Microwaves and Optoelectronics* (Springer, 1998).
31. H. I. Sztul and R. R. Alfano, "The Poynting vector and angular momentum of Airy beams," Opt. Express **16**, 9411–9416 (2008).
32. R. Zambrini and S. M. Barnett, "Quasi-intrinsic angular momentum and the measurement of its spectrum," Phys. Rev. Lett. **96**, 113901 (2006).